remote sensing

MDPI

Article

Development of a New Tropical Cyclone Strip Segment Retrieval Model for C-Band Cross-Polarized SAR Data

Letian Lv [1], Yanmin Zhang [1], Yunhua Wang [1,2], Wenzheng Jiang [3,*] and Daozhong Sun [1]

[1] Faculty of Information Science and Engineering, Ocean University of China, Qingdao 266100, China; lvletian@stu.ouc.edu.cn (L.L.); yanminzhang@ouc.edu.cn (Y.Z.); yunhuawang@ouc.edu.cn (Y.W.); sundaozhong@stu.ouc.edu.cn (D.S.)
[2] Pilot National Laboratory for Marine Science and Technology, Qingdao 266237, China
[3] First Institute of Oceanography, Ministry of Natural Resources, Qingdao 266061, China
* Correspondence: jwzheng668@fio.org.cn; Tel.: +86-158-0658-5420

Abstract: Compared with co-polarized (HH/VV) normalized radar cross-section (NRCS) backscattered from the sea surface, there is no saturation phenomenon in cross-polarized (HV/VH) NRCS when wind speed is greater than about 20 m/s, so cross-polarized synthetic aperture radar (SAR) images can be used for high wind speed monitoring. In this work, a new geophysical model function (GMF) is proposed to describe the relation of the C-band cross-polarized NRCS with wind speed and radar incidence angle. Here, sixteen ScanSAR wide mode SAR images acquired by RADARSAT-2 (RS-2) under tropical cyclone (TC) conditions and the matching wind speed data from the European Centre for Medium-Range Weather Forecasts (ECMWF) and the Stepped-Frequency Microwave Radiometer (SFMR) are collected and divided into datasets A and B. Dataset A is used for analyzing the effects of the wind field and radar incidence angle on the reference noise-removed cross-polarized NRCS, and for proposing the new GMF for each sub-swath of the SAR images, while dataset B is used to retrieve wind speed and evaluate the validity of the new GMF. The comparisons between the wind speeds retrieved by the new GMF and the collocated ECMWF and SFMR data demonstrate the excellent performance of the new GMF for wind speed retrieval. To analyze the universality of the new GMF, wind speed retrievals based on 32 Sentinel-1A/B (S-1A/B) extra-wide-swath (EW) mode images acquired under TC conditions are also compared with the collocated wind speeds measured by the Soil Moisture Active Passive (SMAP) radiometer, and the retrieved wind speeds have RMSE of 3.667 m/s and a bias of 2.767 m/s. The successful applications in high wind speed retrieval of different tropical cyclones again supports the availability of the new GMF.

Keywords: synthetic aperture radar (SAR); cross-polarization NRCS; ECMWF and microwave radiometer wind speed; GMF; tropical cyclone wind speed retrieval

Citation: Lv, L.; Zhang, Y.; Wang, Y.; Jiang, W.; Sun, D. Development of a New Tropical Cyclone Strip Segment Retrieval Model for C-Band Cross-Polarized SAR Data. *Remote Sens.* **2022**, *14*, 1637. https://doi.org/10.3390/rs14071637

Academic Editors: Bryan Stiles, Svetla Hristova-Veleva, Lucrezia Ricciardulli, Larry O'Neill, Zorana Jelenak and Joe Sapp

Received: 29 January 2022
Accepted: 25 March 2022
Published: 29 March 2022

1. Introduction

Tropical cyclones (TCs) produce strong winds, heavy rain, and high sea states in the sea, which pose a serious threat to marine navigation and the lives of coastal residents. The observation of TC wind speed is of major importance for TC monitoring and forecasting [1–3]. In recent years, the retrieval algorithms for the high wind speed of TCs have attracted extensive attention in the satellite oceanic remote sensing field. At present, because of the cloud-penetrating ability, microwave sensors such as radiometers [3,4], scatterometers [5,6], altimeters [7,8], and synthetic aperture radar (SAR) are used for sea surface wind retrieval. The superior high spatial resolution of SAR is advantageous for imaging sea surface changes caused by mesoscale atmospheric processes. The exceptional details on the structure of the sea surface wind field of TCs can be clearly manifested in SAR images of the ocean surface. Therefore, SAR images have been widely investigated for retrieving fine-scale wind fields of TCs [9–11]. The geophysical model functions (GMFs), which are the empirical relations between normalized radar cross-section (NRCS), wind

speed, wind direction, and radar incidence angle, can be used to transform the NRCS from satellite-borne SAR images of the ocean surface into a wind field [9–13]. The GMFs exist just because a wind field would roughen the sea surface via the production of sea waves, which in turn enhance the backscattered NRCS at moderate incidence angles [14–19]. The works in [16–19] demonstrate that the GMFs for co-polarized SAR images have limitations to retrieve tropical cyclone-force wind speed because the co-polarized NRCS would be saturated when sea surface wind speed exceeds 20 m/s. Due to the ability of tracing wave breaking [16–19], recent research on cross-polarized SAR images has shown that the cross-polarized NRCS even remains sensitive to sea surface wind speed under tropical cyclone conditions, which indicates its potential for TC wind speed retrieval [16,18,20,21].

With the development of SAR technology, considerable efforts have been made to quantitatively retrieve sea surface wind speed on the basis of cross-polarized SAR images. At present, several statistical models based on GMFs have been proposed for C-band cross-polarization NRCS [22–29]. In [22,23], two GMFs, i.e., the C-2PO and the C-2POD models, established the linear relationship between cross-polarized NRCS in decibels and wind speed. In [24], it is found that the relationship between cross-polarized NRCS and wind speed had different forms in low-to-strong (<20 m/s) and strong-to-severe ($\geq$20 m/s) wind regimes. In recent years, many studies have shown that the cross-polarized NRCS from the sea surface is not only related to wind speed, but also affected by radar incidence angle [11,25–27]. Some GMF models, such as H14, MS1A, and C3PO, were represented by the functions of wind speed and radar incidence angle. The H14 [25] model was proposed based on the dual-polarization SAR images acquired by RS-2 and the wind speed data from buoys, SFMR, and ECMWF. The MS1A model was established according to the extra-wide-swath SAR images acquired by Sentinel-1A (S-1A) and the wind speeds from SMAP [11,27]. The H14 and MS1A models are both power law functions relating cross-polarized NRCS to wind speeds and radar incidence angles. Based on the RS-2 ScanSAR images and the wind speed from SFMR, the C3PO model, which can be used to retrieve wind speeds up to 40 m/s, was proposed in [26]. The effect of the noise floor of SAR instruments on the GMF is another issue that needs attention. For ScanSAR wide-swath SAR images, the cross-polarized NRCS would be significantly contaminated by the reference noise floor (i.e., the noise equivalent sigma zero, NESZ) [10,11,25,27]. The NESZ varies with the radar incidence angle, and modulates the cross-polarized NRCS, which leads to clearly visible undulating patterns of brighter and darker areas across the range in SAR images [10]. In [28], a segmented GMF model for cross-polarized NRCS was proposed by introducing a denoise procedure to increase the signal-to-noise ratio for SAR measurements. Shen's model is a piecewise linear function relating cross-polarized NRCS in decibels to wind speed, and the two linear segments meet together when the wind speed is 10.1 m/s. Based on the cross-polarized NRCS in the denoised RS-2 ScanSAR wide-swath images acquired over six TCs, Horstmann et al. [29] explored a relationship between the cross-polarized NRCS and wind speeds.

Although many GMFs for cross-polarized NRCS have been developed to retrieve wind speeds, there are still large RMSEs in the sea surface wind inversion results, especially for high wind speeds. Here, we aimed to develop a new GMF model for RS-2 ScanSAR wide-swath cross-polarized NRCS after removing NESZ. In this work, sixteen scenes of RS-2 ScanSAR wide-swath images under the condition of TCs and the matching wind speeds from ECMWF and SFMR were collected and divided into two datasets. Based on dataset A, we established a new GMF model for each sub-swath of the SAR image, represented as a piecewise function of wind speed and radar incidence angle. This new model is called SS-ICM (i.e., strip segmentation model corrected by incidence angle). We validated the effectiveness of the new GMF by comparing the wind speeds retrieved from RS-2 images in dataset B with the matching wind speeds from ECMWF and SFMR. Compared with the wind speed retrieved by other GMF models, the root mean square error (RMSE) and the bias of the retrieved wind speed based on SS-ICM model are both improved to a certain extent. To further analyze the universality of the new model, wind speed retrievals based

on 32 denoised Sentinel-1A/B (S-1A/B) extra-wide-swath (EW) images were also compared with the collocated wind speeds measured by the SMAP radiometer. The results illustrate that the new GMF has advantages in TC wind speed retrieval.

The remainder of this article is organized as follows. The dataset and data processing methods are described in Section 2. The new GMF model is established in Section 3. The discussion and validation of this model are given in Section 4. Finally, we present our conclusions in Section 5.

2. Description of Datasets

2.1. SAR Data

Canada's RADARSAT-2 is a high-resolution commercial satellite with C-band sensors, offering a variety of polarization modes including single-polarization (VV, HH, VH, or HV), dual-polarization (VV+VH, or HH+HV), and quad-polarization (VV+HH+VH+HV) [10,20,30]. Among them, ScanSAR wide dual-polarization (VV+VH) data can capture complete and clear TC information due to its wide swath with a width of 500 km. The spatial resolution of ScanSAR wide mode SAR image is 100 m $\times$ 100 m and the pixel spacing is 50 m $\times$ 50 m, and the radar incidence angle range is 20° to 49°. For RS-2 ScanSAR wide mode SAR images, sixteen SAR images containing TCs are selected and divided into dataset A (includes 13 SAR images) and dataset B (includes three SAR images). Dataset A is utilized to analyze the relationship between the cross-polarized NRCS and wind speed, wind direction, and radar incidence angle, and then to fit the wind speed retrieval model. Dataset B is a validation dataset used to verify the performance of the proposed wind speed retrieval model. Both datasets were sampled, and outliers outside the 95% confidence interval were removed. At the same time, the data with rainfall rates over 30 mm/h were also removed to avoid the impact of rain damping caused by heavy rainfall on NRCS. The same process was performed for 32 scenes of S-1 SAR data. The specific information of the RS-2 ScanSAR wide mode images used in this paper is shown in Table 1.

Table 1. Information of the RADARSAT-2 ScanSAR wide-mode images.

Number	Name	Imaging Time (UTC)	The Comparison of Data	Dataset
1	Eral	2010-09-02, 22:59:14	EC, SFMR [2]	A
2	Arthur	2014-07-03, 11:13:56	EC, SFMR [2]	A
3	Harvey	2017-08-25, 00:19:57	EC	A
4	Lan	2017-10-21, 09:20:57	EC	A
5	Suli	2018-08-18, 08:02:33	EC, SMAP	A
6	Suli	2018-08-20, 21:05:21	EC, SMAP	A
7	Jebi	2018-09-02, 09:04:49	EC, SMAP	A
8	Flossie	2019-08-01, 14:33:48	EC	A
9	Genevieve	2020-08-21. 13:31:53	EC, SMAP	A
10	Haishen	2020-09-02, 08:41:51	EC	A
11	Teddy	2020-09-21, 10:04:32	EC, SFMR [1], SMAP	A
12	Epsilon	2020-10-24, 21:56:22	EC, SMAP	A
13	Zeta	2020-10-28, 12:07:10	EC, SFMR [2]	A
14	Joaquin	2015-10-03, 10:44:58	EC, SFMR [1], SMAP	B
15	Florence	2018-09-13, 10:59:32	EC, SFMR [1], SMAP	B
16	Michael	2018-10-09, 11:43:42	EC, SFMR [2]	B

[1] The image contains only one set of SFMR data. [2] This image contains two groups of SFMR data.

Sentinel-1A/B satellites [10,11], designed by the European Space Agency (ESA), can be operated in four exclusive sensor modes with different resolutions and coverage: the strip-map mode (SM), the interferometric wide-swath mode (IW), the extra-wide mode (EW), and the wave mode (WV). An EW mode SAR image is 400 km wide and covers radar incidence angles from about 19° to 47°, with spatial resolution of 93 m × 87 m and pixel spacing of 40 m × 40 m. In this paper, 32-scene Sentinel-1 EW mode dual-polarization (VV+VH) Ground Range Detected (GRD) Medium-Resolution (MR) SAR images acquired over TCs are also selected as a validation dataset to analyze the universality of the new GMF model. Due to the large amount of S-1 SAR data, we do not list them.

In this paper, the cross-polarized NRCS without reference noise (see Section 2.6.3 for details) from the two satellite platforms is smoothed with a mean filtering window of 50 pixels × 50 pixels to remove the influence of speckle noise. At the same time, the land area in SAR images was assigned an invalid value and removed to eliminate the influence of land on the cross-polarization NRCS.

2.2. The Fifth-Generation Reanalysis Wind Field of ECMWF

ERA5 is the fifth generation of the European Center for Medium-Range Weather Forecasts (ECMWF) reanalysis database [31–33]. In this study, from ECMWF-ERA5, we select the wind speed at a height of ten meters above sea surface as the 'true' wind fields. The time and the spatial resolutions of the reanalysis wind field are 1 h and 0.25 × 0.25 degrees [34]. In our study, the ECMWF data are interpolated to SAR imaging time Meanwhile, the spatial resolution of the ECMWF wind fields is also interpolated at less than 0.01°. This ensures ECMWF data are spatially matched with the smoothed SAR images.

2.3. SFMR Measurements

In 2005, the National Oceanic and Atmospheric Administration (NOAA)/Aircraft Operations Center (AOC) first used a Stepped-Frequency Microwave Radiometer (SFMR) on the WP-3D research aircraft for actual measurements of hurricane surface wind speeds [35–38] and rain rates [39,40]. The SFMR is a C-band microwave radiometer that works at six frequency bands (4.55, 5.06, 5.64, 6.34, 6.96, 7.22 GHz) and can be used to retrieve the 1-min sustained ground wind speeds, with the measured maximum wind speeds up to 70 m/s. The wind data acquired by the SFMR have high spatial (120 m) and temporal (1 Hz) resolutions. When comparing the performance of the SFMR data and SAR data, the average wind speed within ±0.01° latitude and longitude of the SAR image corresponding to the flight track is selected to reduce the error.

2.4. L-Band SMAP Radiometers Data

The soil moisture active passive (SMAP) L-band SAR has captured ample data since the National Aeronautics and Space Administration (NASA) launched it in January 2015 and provided data since April 2015. The spatial resolution of SMAP wind speed is 0.25° × 0.25°. It has a strip width of 1000 km and can cover the global sea in 2–3 days [41,42]. The SMAP radiometer is derived from brightness temperature retrieval and has been proven to be an efficient microwave sensor for observing ocean surface winds [3,4,43–45]. The SMAP radiometer can accurately estimate hurricane intensity (70 m/s) and wind radius, and the wavelength of the L-band is much larger than the radius of a raindrop, so high wind speed can be measured even under heavy rainfall conditions [43].

2.5. The Hurricane Track Data

In order to better match the airborne SFMR wind speed with SAR images, the track information of TCs is needed. The best track data were obtained from the international best-track archive for climate stewardship (IBTrACS_v04) dataset in the National Oceanic and Atmospheric and Administration (NOAA), which combined structural estimates of the best tropical cyclone track data from multiple agencies around the world [3,27]. The IBTrACS data are widely used to verify the model prediction of TC track and intensity

and analyze the global changes in hurricane moving velocity and life cycle [46–48]. It has provided information on 13,550 TCs since 1842, including the longitude and latitude of the eye center, maximum wind speed, time, and so on, with a set of data every three hours.

2.6. Data Processing and Matching

2.6.1. Flight Path Correction of Airborne SFMR Measurements

It is essential to consider the motion of TCs when matching the position of SFMR data on SAR images. Correcting the SFMR flight path requires obtaining TC track data. The new positions of the TC's eye at different moments corresponding to SFMR data are obtained by linear interpolation. Then, shifting the flight path of SFMR on the basis of the displacements between the original and the new positions of the TC's eye, the modified SFMR path on the SAR image is obtained. Figure 1 shows the SAR image of the TC Earl. In this study, the SFMR data and SAR data were matched to within the 1-hour window. The aircraft entered the SAR imaging area at 21:59:14 UTC and left at 23:59:14 UTC, and passed through the eye of the TC. In Figure 1, the blue line is the corresponding flight track of the SFMR, and the red line denotes the modified aircraft flight track. The arrows indicate the direction of the aircraft.

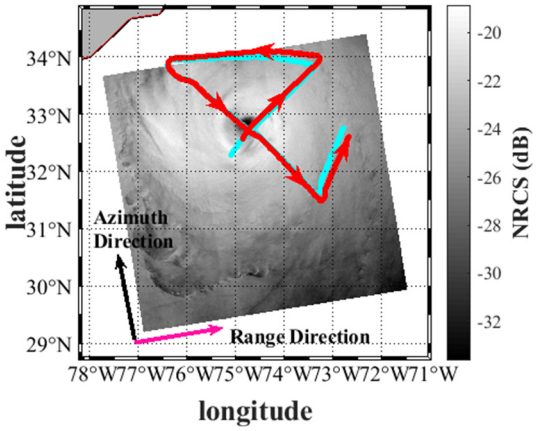

Figure 1. The RS-2 SAR image of TC Earl on 2 September 2010, at 22:59:14 UTC. The black and pink arrows denote the azimuth and range directions of the SAR image, respectively. The blue line represents the original SFMR track, and the red line denotes the modified SFMR track by considering the TC's movement.

2.6.2. Judgment and Selection of Fitting Data

To prove the accuracy of the ECMWF wind field, the comparison between the NDBC in situ data and the interpolated ECMWF reanalysis wind speeds are shown in Figure 2a. Here, we analyzed five years of data measured by the buoy (No. 41047) from 2016 to 2020, collecting 40,552 wind speed data points in total. The root mean square error (RMSE) is 1.15 m/s, and the bias is 0.831 m/s. The wind speed of the buoy and ECMWF were concentrated below 20 m/s, and they showed a good correlation.

However, as shown in Figure 2a, there are few wind speeds over 20 m/s, and we cannot rely on buoy 41,047 to determine whether ECMWF data are still appropriate under high wind speed conditions. Therefore, the collocated wind speeds from the SMAP radiometer in datasets A and B are compared with ECMWF data in Figure 2b. It can be found that when the wind speeds are lower than 20 m/s, ECMWF wind speeds have a good linear relationship with SMAP wind speeds, which are approximately evenly distributed on both sides of the diagonal. This means that the ECMWF data can maintain adequate retrieval accuracy in the middle and low wind speed regions. However, when the wind speeds keep increasing, ECMWF wind speeds are obviously lower than those from SMAP, which means that using ECMWF data as the real wind fields for establishing the TC retrieval model for high wind speeds will cause relatively large errors. Therefore, when we establish a GMF

model, a threshold wind speed is set to be 22 m/s. When the wind speed exceeded 22 m/s, wind speeds acquired by radiometer are selected to establish the GMF for high wind speeds. Compared with SMAP wind speeds, ECMWF wind speed has a large data volume and wide coverage, so ECMWF wind speeds below 22 m/s are still used to establish the GMF for middle and low wind speeds.

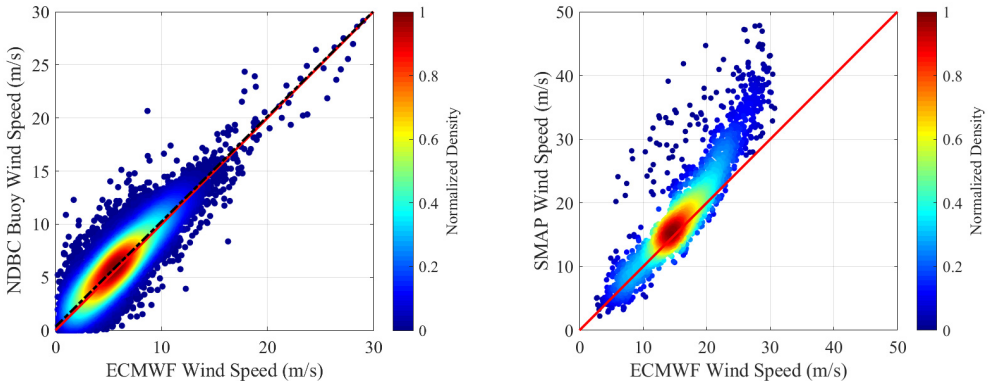

(**a**) (**b**)

Figure 2. Comparison of ECMWF wind speed with (**a**) the in situ measurements of NDBC buoy data (NO. 41047), (**b**) the measurements of the SMAP radiometers.

2.6.3. Correction of Reference Noise

RS-2 ScanSAR wide and S-1 EW mode SAR images give a reference noise level (i.e., the noise equivalent sigma zero, NESZ) values between −30 dB and −23 dB depending on the radar incidence angle [10,29]. The signal-to-noise ratio (SNR) of cross-polarized SAR images is relatively low and strongly influenced by NESZ, which makes the cross-polarized SAR images have obvious changes of brighter and darker bands along the range direction. After removing the reference noise, the cross-polarized NRCS σ_{VH} in decibels can be evaluated by

$$\sigma_{VH} = 10\log_{10}(\sigma_{linear} - Nosie\_\sigma_{linear}) \quad (1)$$

where σ_{linear} denotes the NRCS contaminated by reference noise. $Nosie\_\sigma_{linear}$ denotes the NESZ. σ_{linear} and $Nosie\_\sigma_{linear}$ are both in linear unit. The values of the NESZ can be found in the header file of SAR images.

Figure 3 shows an example of a RS-2 cross-polarized SAR image of TC Teddy acquired on 21 September 2020, at 10:04:32 UTC, when a clear eye of this tropical cyclone was captured. From this SAR image without removing the NESZ (see Figure 3a), the obviously bright and dark bands can be seen in the range direction. Same as [29], we select a sub-image with the size of 2000 pixels (100 km) along the azimuth direction, as shown in the red box in Figure 3a. The sub-image is processed with Equation (1) to remove the NESZ. It can be seen from Figure 4b that, after subtracting the contribution of the NESZ from the NRCS, the phenomenon of fluctuation along the range direction disappears to a large extent. However, when NESZ is removed by using the processing method in [29], there are still three obvious splicing lines in the SAR image along the azimuth direction due to the existence of strip splicing. To address this problem, the NRCS along the splicing line is replaced by the interpolated value of the data from both sides of the splicing line. Then, the influence of strip splicing can be eliminated completely (see Figure 4c).

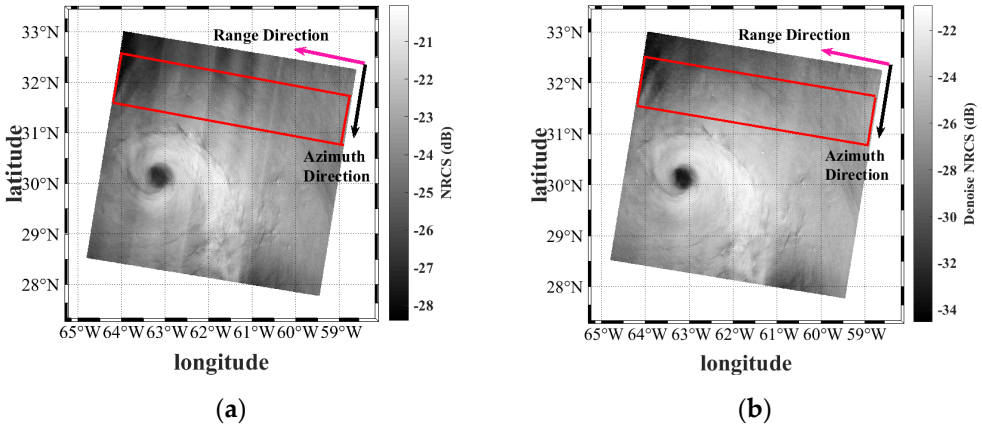

Figure 3. The RS-2 SAR image of TC Teddy on 2 September 2020, at 10:04:32 UTC. Red square denotes the selected sub-image. (**a**) The original SAR image, and (**b**) the SAR image after removing the influence of NESZ and strip splicing.

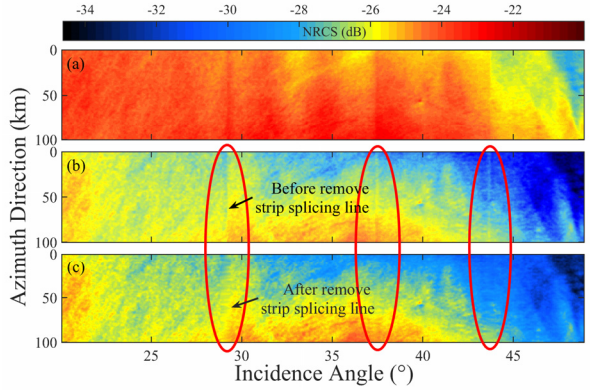

Figure 4. Sub-image in the red box range in Figure 3. (**a**) Original NRCS, (**b**) NRCS after removing the NESZ, and (**c**) NRCS after removing the NESZ and strip splicing.

Figure 5 shows the dependence of cross-polarized NRCS with radar incidence angle before and after removing NESZ. The green line represents the result of azimuth-averaged original NRCS in sub-image (see Figure 4a). It can be clearly seen that the fluctuation trend of original NRCS is similar to that of the NESZ, especially in the W2 and W30 bands, which indicates that the original NRCS is seriously contaminated by the reference noise. When the effect of NESZ is subtracted, NRCS decreases by about 2–6 dB. Similar processing was also performed in the literature [29], but the author did not take into account the influence of strip stitching, which led to the mutation of NRCS in SAR images. When we remove the influence of strip splicing, from the comparison between the red and the blue curves, it is obvious that the mutations at the strip splices disappear completely.

For Sentinel-1 data, the NESZ distributed in the range direction and the wavelike modulation of NRCS (scalloping effect) along the azimuth direction can be obtained from the header file. The influence of these two kinds of reference noise can be directly removed by the calibration formula:

$$\sigma_{VH} = 10 \log_{10}\left(\frac{DN^2 - na \cdot nr}{A^2}\right) \quad (2)$$

where DN^2 is SAR image intensity, A is the scaling coefficient, and na and nr represent the values of the scalloping and NESZ, respectively.

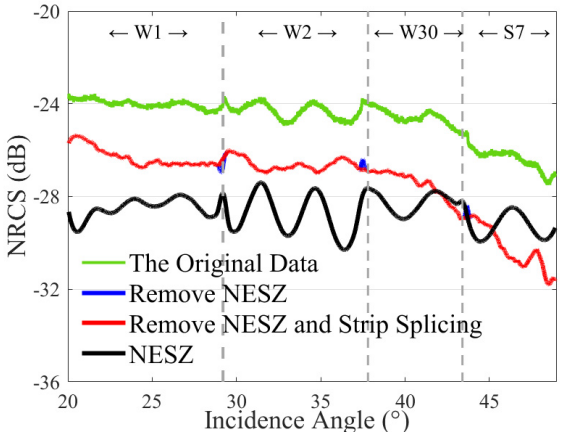

Figure 5. Influence of the reference noise on the cross-polarized NRCS. The black curve is the NESZ. The green curve is the original NRCS, while the blue curve denotes the NRCS after removing the reference noise. The red curve indicates the result after removing the NESZ and strip splicing. The vertical dashed gray lines denote the dividing lines of the four strips: W1, W2, W30, and S7.

3. Establishment of the New GMF

3.1. Training Dataset Analysis

In order to establish a suitable GMF for TC wind speed retrieval, the influence of wind speed, wind direction, and radar incidence angle on the cross-polarized NRCS should first be analyzed. The ECMWF reanalysis wind speed below 22 m/s and SFMR wind speed above 22 m/s are selected as the real wind speeds.

3.1.1. Influence of Relative Wind Direction on Cross-Polarized NRCS

In this work, the data with a radar incidence angle of 35° are selected. The whole relative wind direction (0–360°) is evenly divided into 36 bins. The curves of the cross-polarized NRCS for different wind speeds are shown in Figure 6. The relative wind direction denotes the angle between wind direction and the SAR range direction, considering that 0° is upwind, 180° is downwind, and 90° and 270° denote crosswind directions. Although some studies [12,29] have shown that there is a weak relationship between cross-polarized NRCS and wind direction when the wind speed is low, the curves in Figure 6 illustrate that this relationship is chaotic and fuzzy. In the following model construction process, therefore, the effect of the wind direction has been ignored.

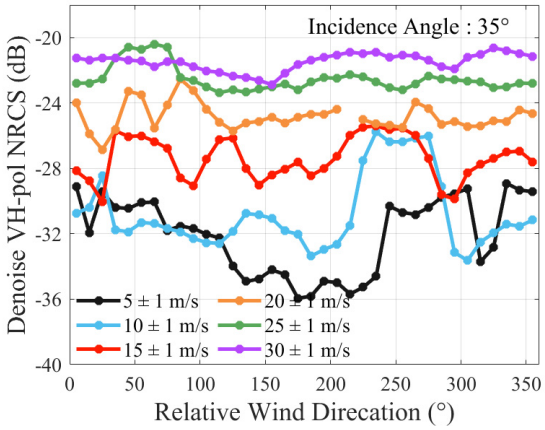

Figure 6. Influence of wind direction on the cross-polarized NRCS for different wind speeds.

3.1.2. Influence of Incidence Angle on Cross-Polarized NRCS

Some analysis in [11,25,26] shows the dependence of cross-polarized NRCS on the incidence angle. Here, the incidence angle of the RS-2 ScanSAR mode image ranges from

20° to 49°. All SAR image data under downwind conditions are grouped into six even incidence angle bins. Then, the average cross-polarized NRCS for different wind speeds in each bin are extracted and plotted successively in Figure 7. The curves in this figure show that the values of the cross-polarized NRCS for different wind speeds tend to decrease with the increase in incidence angle, which is consistent with the conclusion in [11,25,26]. The same conclusion can be drawn for other wind direction cases, too. This phenomenon means that the influence of the radar incidence angle on the cross-polarized NRCS must be considered in the modeling process of the new GMF.

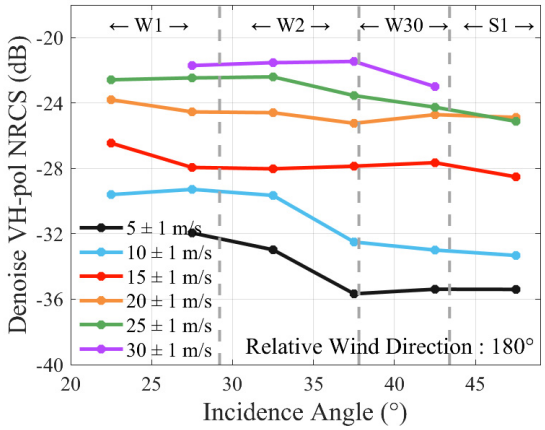

Figure 7. Influence of the incidence angle on cross-polarized NRCS for different wind speeds.

3.1.3. Influence of Wind Speed on Cross-Polarized NRCS

A number of literary studies have shown that cross-polarized NRCS has a positive correlation with wind speed even when wind speed is higher than 20 m/s, so it is often used for the retrieval of high wind speed [22–29]. Figure 8a,b present the influences of the wind speed on cross-polarized NRCS for different incidence angles and different wind directions. As shown in Figure 8, the cross-polarized NRCS monotonically increase with the increase in wind speed. At moderate winds, the values of the cross-polarized NRCS are most sensitive to wind speed. When the wind speed is low, the values of the cross-polarized NRCS increase slowly with wind speed. This phenomenon can perhaps be explained by the fact that the signal-to-noise ratio of the cross-polarized NRCS in the low-wind region is too low. Although the reference noise reduction is carried out, the effect of the noise signal cannot be completely removed. When the wind speed exceeded about 20 m/s, the cross-polarized data present a trend of slow increase with wind speed again. This change trend is apparently closer to the empirical relationships proposed by Hwang et al. [25] and Mouche et al. [11,27]. From Figure 8a, we can also find that the cross-polarized NRCS tend to decrease with the increase in incidence angle. Compared with Figure 8a, however, the curves for different wind directions in Figure 8b are mixed together and difficult to distinguish, which means that there is no obvious correlation between cross-polarized NRCS and wind direction.

3.2. The New GMF Model

From the analysis in Section 3.1, it is found that the denoised cross-polarized NRCS would be affected by wind speed and radar incidence angle, and the relationship between the cross-polarized NRCS and wind speed cannot be described by a simple linear function. Therefore, in this section, we try to establish a new piecewise wind speed retrieval model for each sub-swath of SAR images. Hereafter, this new model is referred to as SS-ICM (i.e., strip segmentation model corrected by incidence angle). The SS-ICM model can be expressed as:

$$\sigma_{VH} = \sigma_v f_\theta \quad (3)$$

where σ_{VH} denotes the cross-polarized NRCS in decibels, σ_v is a function of wind speed, which represents the relationship between NRCS and wind speed, and f_θ is an incidence angle correction function. During the establishment of the SS-ICM model, the training data in dataset A were divided into four groups according to the sub-swaths W1 ($\theta < 29.2°$), W2 (29.2–37.8°), W30 (37.8–43.4°), and S7 ($\theta > 43.4°$). The samples numbers are 3658, 2868, 2219, and 2495 in the sub-swaths W1, W2, W30, and S7, respectively.

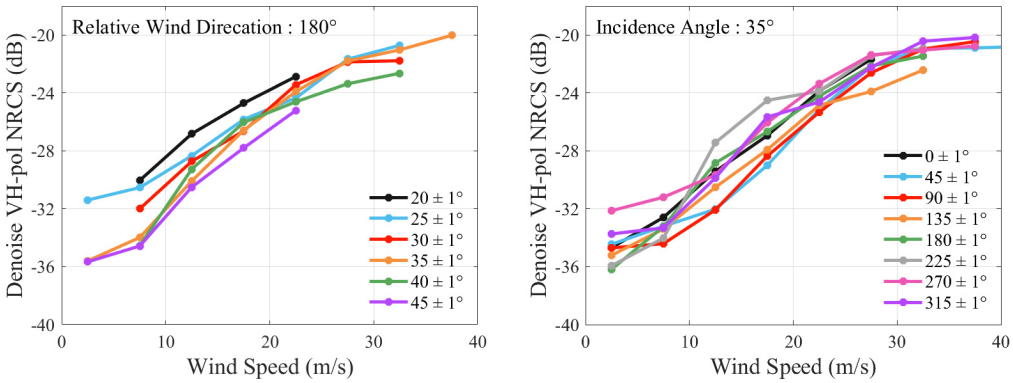

(**a**) (**b**)

Figure 8. Influence of wind speed on the cross-polarized NRCS for (**a**) different incidence angles when the relative wind direction is 180°, and (**b**) different relative wind directions when the incidence angle is 35°.

3.2.1. Wind Speed Function σ_v

In combination with the ECMWF wind speeds below 22 m/s and the SFMR measurement data above 22 m/s, the cross-polarized NRCS in each sub-swaths as a function of wind speeds are shown in Figure 9. For comparisons, the cross-polarized NRCS evaluated by the GMFs proposed by Horstmann et al. [29], Hwang et al. [25], and Mouche et al. [11,27] are also presented. From the comparisons, we found that these four GMFs display significantly different behaviors, and the four existing GMFs cannot adequately describe the relationship between the cross-polarized NRCS of each sub-swath and wind speed.

Due to the complex trend of cross-polarized NRCS with wind speed, it is difficult to establish a unified fitting function for cross-polarized NRCS at different wind speed ranges and different sub-swaths. In order to fit the scatters in Figure 9 well, we divide the cross-polarized NRCS into three wind speed ranges with the two vertical dotted lines in Figure 9.

The first wind speed range corresponds to low wind speed cases. In the sub-swaths W1, W2, and W30, the upper threshold wind speed for the first wind speed range is 11.5 m/s. In the sub-swath S7, the upper threshold wind speed is set 10.0 m/s. In this wind speed range, the sensitivity of cross-polarized NRCS to wind speed increases with wind speed, and a quadratic function can be employed to fit the scatters well. Compared with the NRCS at low wind speed, the cross-polarized NRCS is more sensitive to wind speed in a moderate wind speed range, where the wind speed ranges from 11.5 m/s to 19 m/s in W1 and W2, from 11.5 m/s to 20 m/s in W30, and from 10 m/s to 22 m/s in S7. At moderate wind speeds, the scatterplots in Figure 9 show that the cross-polarized NRCS in each sub-swath almost increases linearly with the increase in wind speed. Therefore, at moderate wind speeds, a linear function of wind speed can be used to fit the NRCS data. When the wind speed continues to increase, the cross-polarized NRCS flattens out again with the increase in wind speed. Because the sensitivity of cross-polarized NRCS to wind speed decreases with high wind speed, a power function is chosen to ensure the trend of the cross-polarized NRCS at high wind speed.

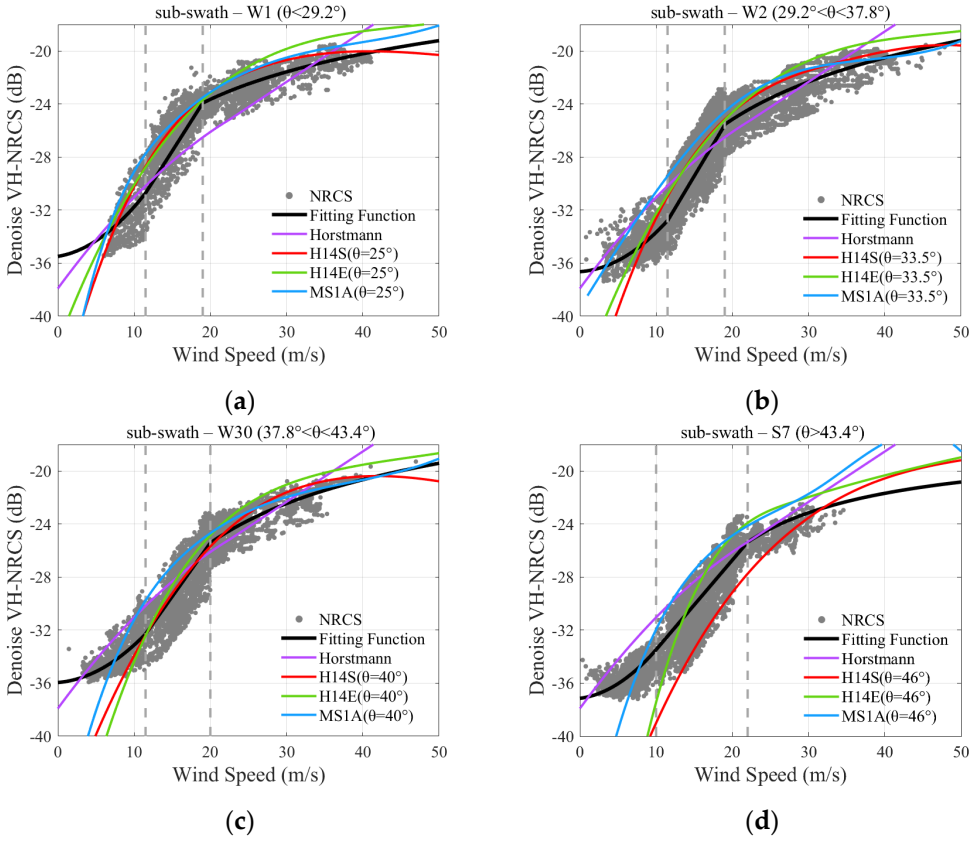

Figure 9. Relationship between the cross-polarized NRCS and the wind speed on the sub-swaths (**a**) W1, (**b**) W2, (**c**) W30, and (**d**) S7. The black lines denote the fitting curves.

Based on the above analysis, the fitting function σ_v of the cross-polarized NRCS with wind speed is established as:

$$\sigma_v = \begin{cases} A_1 v^2 + B_1 v + C_1 & (v < v_1) \\ B_2 v + C_2 & (v_1 \le v < v_2) \\ A_3 \left(v^{B_3}\right) + C_3 & (v \ge v_2) \end{cases} \quad (4)$$

where v denotes the wind speed, and the coefficients in Equation (4) are given in Table 2.

Table 2. List of the coefficients in Equation (4).

Sub-Swath	v_1 (m/s)	v_2 (m/s)	i	A_i	B_i	C_i
W1	11.5	19	1	0.02768	0.09696	−35.49
			2		0.9062	−41.1356
			3	−46.57	−0.2263	0
W2	11.5	19	1	0.02578	0.03866	−36.64
			2		0.9664	−43.8995
			3	−60.89	−0.2951	0
W30	11.5	20	1	0.02355	0.04711	−35.95
			2		0.8088	−41.5949
			3	−68.92	−0.4558	−7.826
S7	10	22	1	0.02927	0.07417	−37.142
			2		0.6759	−40.2318
			3	0.02768	0.09696	−35.49

3.2.2. Incidence Angle Correction Function f_θ

From the discussion in Section 3.1.2, it can be inferred that the change in incidence angle has a certain impact on the cross-polarized NRCS. In order to consider the influence of the radar incidence angle, in the new GMF, an incidence angle correction function f_θ is employed to optimize the wind speed model σ_v. Using the actual cross-polarized NRCS σ_{VH_Actual} from SAR images and the cross-polarized NRCS evaluated by Equation (4), the values of the incidence angle correction function can be calculated by the ratio $\sigma_{VH\_Actual}/\sigma_v$. The values of the ratio are shown in Figure 10. From the scatterplot, we can find that the relationships between the ratio $\sigma_{VH\_Actual}/\sigma_v$ and the incidence angle in the four sub-swaths are different from each other. The fitting function of the ratio $\sigma_{VH\_Actual}/\sigma_v$ for each sub-swath is given by Equation (5). The values of the incidence angle correction function evaluated by Equation (5) are represented by the light blue lines in Figure 10.

$$f_\theta = \begin{cases} a\theta^2 + b\theta + c & \text{for sub-swath W1} \\ b\theta + c & \text{for sub-swath W2, W30 and S7} \end{cases} \quad (5)$$

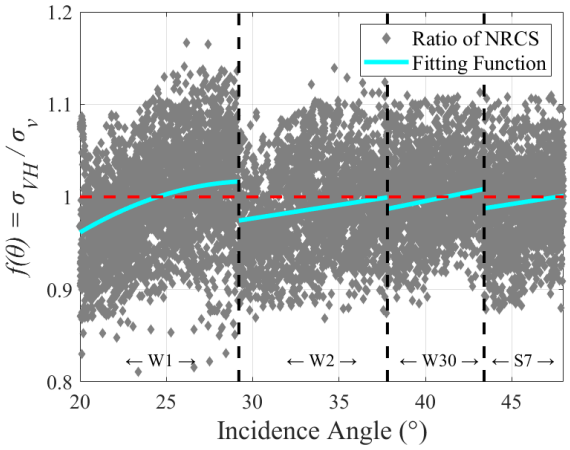

Figure 10. The values of the incidence angle correction function. The rhombuses denote the values evaluated by $\sigma_{VH\_Actual}/\sigma_v$. The light blue lines denote values calculated by the fitting function (5), the red dotted line represents the value of $f_\theta = 1$, and the three vertical black dotted lines represent the boundaries of the four sub-swaths.

The coefficients in Equation (5) are given in Table 3.

Table 3. List of the coefficients in Equation (5).

Sub-Swath	Incidence Angle (°)	*a*	*b*	*c*
W1	$\theta < 29.2$	−0.0005462	0.03286	0.5228
W2	$29.2 \leq \theta < 37.8$		0.004523	0.8295
W30	$37.8 \leq \theta < 43.4$		0.001811	0.9236
S7	$\theta \geq 43.4$		0.001859	0.9133

4. Validation and Discussion

In order to evaluate the performance of the SS-ICM model, the RS-2 cross-polarized NRCS of dataset A and dataset B are used to retrieve wind speeds by this model. The retrieval results are compared with the wind speed from the ECMWF, the airborne SFMR, and the SMAP. In addition, the applicability of the SS-ICM model is also analyzed by applying the model to wind speed retrieval for S-1 satellite SAR data.

4.1. Optimization Performance Evaluation of the SS-ICM Model

The errors between the NRCS calculated by the new GMF model and the SAR observed values are compared in Figure 11, where the abscissa is the real NRCS observed by RS-2, the ordinate denotes the NRCS calculated by the GMF model, the blue dots are the results calculated by Equation (4), and the red dots are the result obtained by Equation (3), i.e., the SS-ICM model. Compared with the real NRCS observed by RS-2, the RMSE and the bias of the results calculated by SS-ICM model both decrease when the incidence angle correction function is considered. This indicates that considering the impact of incidence angle is helpful to improve the model's accuracy.

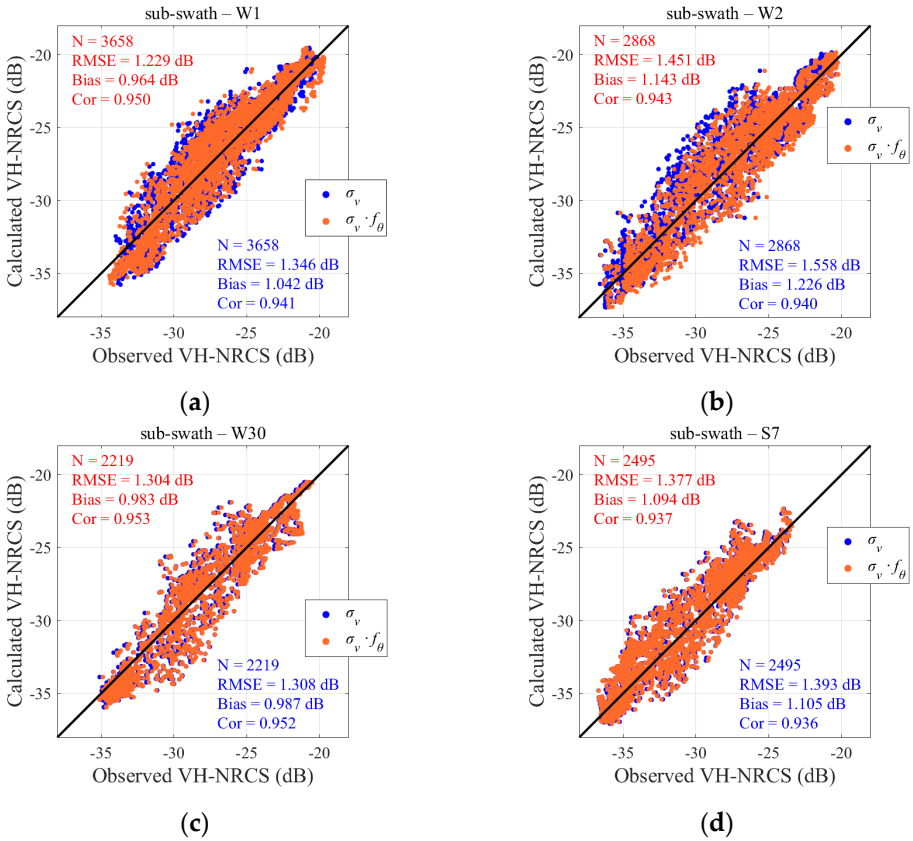

Figure 11. NRCS before and after correction using incidence angle model vs. NRCS observed by radar without NESZ on the sub-swaths (**a**) W1, (**b**) W2, (**c**) W30, and (**d**) S7.

4.2. Comparison with the Retrieval Results of Dataset A

In this section, the SS-ICM model is used to retrieve wind speed for cross-polarized NRCS in dataset A, and the retrieval results are compared with the 'real' wind speed in Figure 12. Figure 12a shows the retrieval results by the SS-ICM model. The retrieval results are evenly distributed on both sides of the diagonal, and the black fitting dotted line is very close to the diagonal, which means that the SS-ICM model proposed in this paper has a small deviation compared with the real wind speed in dataset A. For comparisons, the wind speed retrieved based on the models proposed by the Shen model [28], Horstmann model [29], C3PO model [26], H14 model [25], and MS1A model [11,24] are also shown in Figure 12b–f, respectively. The statistical RMSE, bias, and correlation coefficient are given in Table 4. It shows be noted that the H14 model used in this paper is the combination of the H14E model below 22 m/s and the H14S model above 22 m/s.

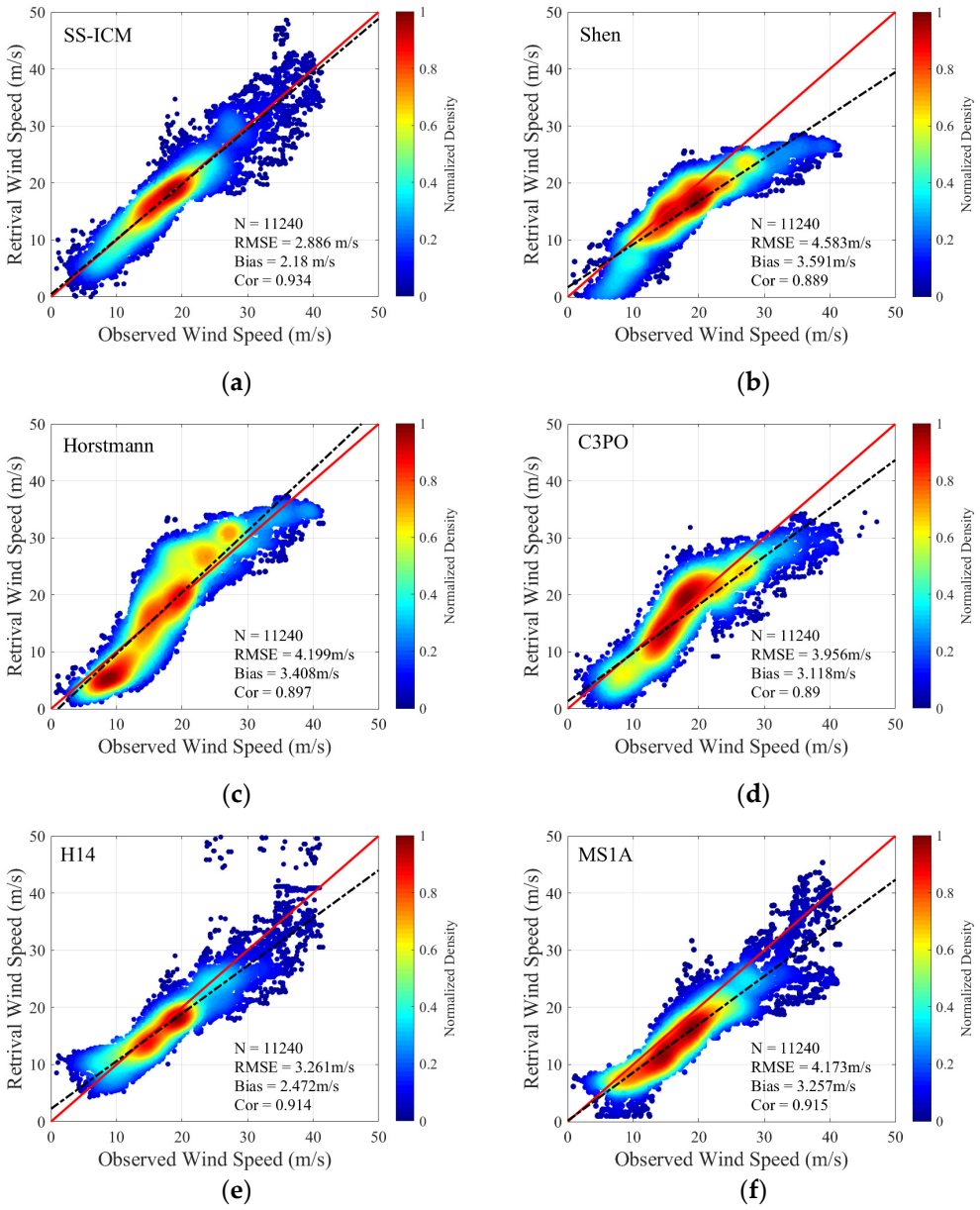

Figure 12. The retrieved wind speeds with (**a**) SS-ICM model; (**b**) Shen model; (**c**) Horstmann model; (**d**) C3PO model; (**e**) H14 model; (**f**) MS1A model in dataset A vs. the 'real' wind speeds.

Table 4. The RMSE and bias of the retrieved wind speeds based on different GMFs.

Model	RMSE (m/s)	Bias (m/s)	Cor
SS-ICM	2.886	2.18	0.934
Shen	4.583	3.591	0.889
Horstmann	4.199	3.408	0.897
C3PO	3.934	3.057	0.902
H14	3.261	2.472	0.914
MS1A	4.173	3.257	0.915

By comparison, the retrieval wind speeds by the SS-ICM model, H14 model, and MS1A model are more consistent with wind speeds in dataset A, especially at the high wind speeds. Among them, SS-ICM model has the highest retrieval accuracy; the RMSE of the retrieved wind speeds reaches 2.886 m/s, the bias is 2.18 m/s, and the correlation coefficient is 0.934. However, it is worth noting that the acceptable inversion results of

SS-ICM only prove the accuracy of the fitting process of this model because it is just fitted based on dataset A. As shown in Figure 12, the Shen model performs well at moderate wind speeds, but the wind speeds are underestimated when the actual wind speed is below 10 m/s or above 20 m/s. For the results of the Horstmann model, when the wind speed is less than 13 m/s, the retrieval wind speeds are somewhat lower than the ECMWF reanalysis wind speed. However, at the wind speed range from 20 m/s to 30 m/s, the wind speeds are overestimated by the Horstmann model. When the wind speed is higher than 30 m/s, the wind speeds would be underestimated by the C3PO model.

4.3. Comparison with the Retrieval Results of Dataset B

In this section, dataset B is used to verify and evaluate the performance of the model proposed in this paper. Compared with some typical wind speed retrieval models, the advantages and disadvantages of SS-ICM model are explored. Dataset B includes the SAR images acquired over three TCs: TC Joaquin captured on 3 October 2015 at 10:44:58 UTC, TC Florence captured on 13 September 2018 at 10:59:32 UTC, and TC Michael captured on 9 October 2018 at 11:43:42 UTC. The TC structures in these three SAR images are very clear. Four groups of SFMR airborne wind speed data in the SAR imaging were located. Similarly, the SS-ICM model and other GMFs mentioned in Figure 12 are used to retrieve wind speeds from these three SAR images. When the retrieval wind speeds are lower/higher than 22 m/s, the retrieval results are compared with the ECMWF/SFMR data, respectively.

4.3.1. Comparison of Retrieval Results with Wind Speeds from ECMWF and SFMR

Taking TC Joaquin as an example, the retrieved wind speed based on different GMFs are shown in Figure 13. Figure 13a is the SAR image of TC Joaquin, including the flight trajectory of the SFMR radiometer. The corresponding ECMWF reanalysis wind field is given in Figure 13b. Figure 13c–i shows the wind speeds retrieved by different GMFs. In Figure 13b, the maximum wind speed of ECMWF is about 25 m/s. Except the retrieved wind speed based on the Shen model, the maximum wind speed retrieved by the other GMFs are all exceed 35 m/s. The pattern of the wind speeds retrieved by the SS-ICM model in Figure 13c is more consistent with those in Figure 13g,i. Since the C3PO model does not remove the influence of the NESZ, the light and dark fringes along the range direction can be clearly identified in Figure 13f. These light and dark fringes have significant effects on the accuracy of wind speed retrieval.

The comparison between the retrieval results and the SFMR wind speed is shown in Figure 14. Comparing the curves in Figure 14, we can find that the low resolution makes the wind speed from ECMWF obviously smoother and the scale of TC eye in ECMWF data is much larger. The maximum wind speed given by ECMWF data is lower than 25 m/s, while the maximum wind speed measured by the SFMR radiometer exceeds 40 m/s. When the wind speed is below 22 m/s, the wind speeds retrieved by SS-ICM, C3PO, and H14 models are in good agreement with the SFMR wind speeds, while the retrieval results of Shen, Horstmann, and MS1A models are slightly lower. When the wind speed is higher than 22 m/s, the wind speeds retrieved by SS-ICM and MS1A models near the eye of the TC are consistent with the SFMR data.

In order to analyze the performance of the GMF models statistically, the wind speeds retrieved from the three SAR images are compared with the ECMWF (below 22 m/s) and the SFMR (above 22 m/s) wind speeds in Figure 15. The statistical RMSE, bias, and correlation coefficient are given in Table 5. Here, the outliers outside the 95% confidence interval have been removed. From the comparisons, we can find that the wind speeds retrieved based on SS-ICM have the smallest RMSE and bias.

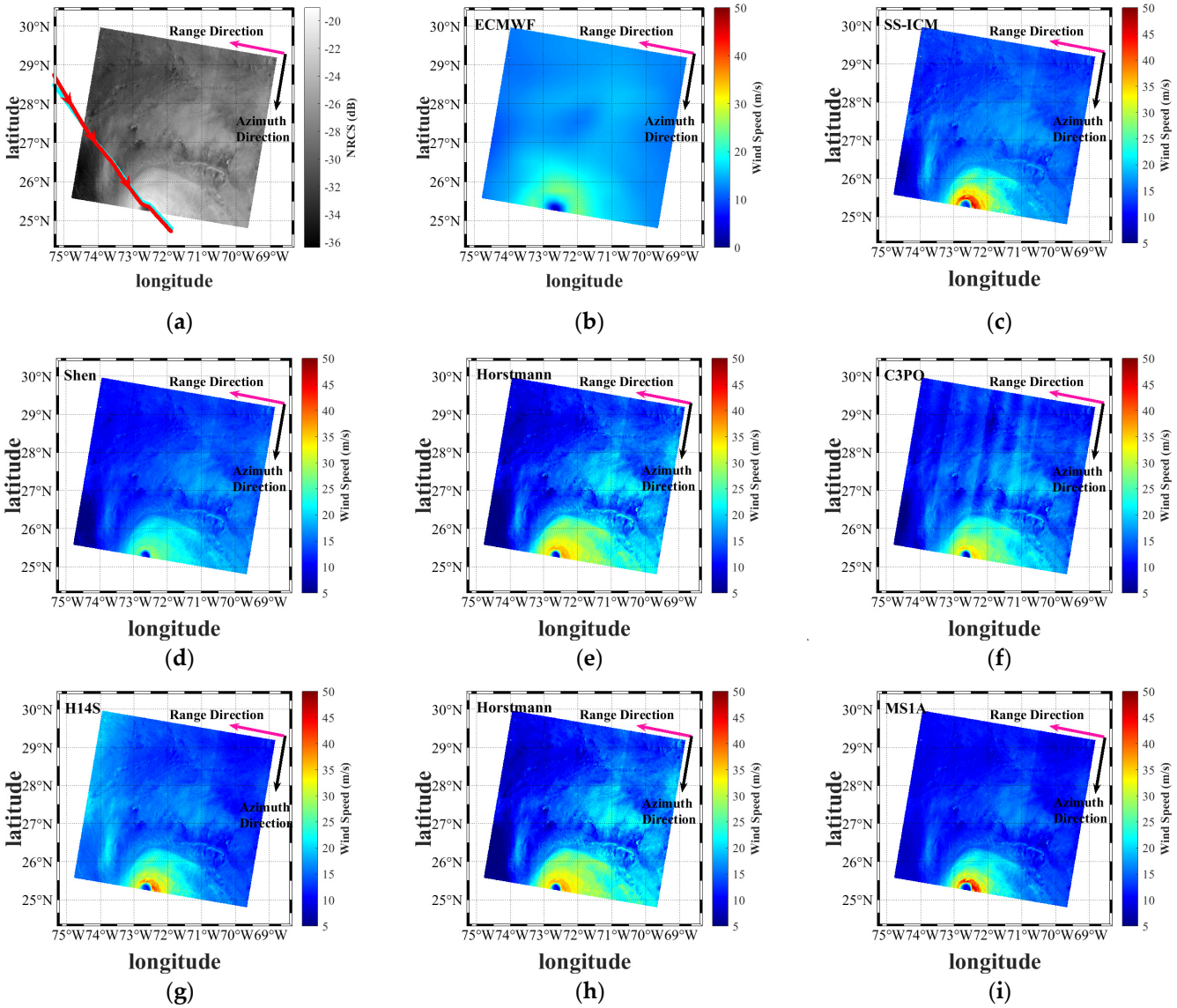

Figure 13. The wind speed retrieved by different GMFs. (**a**) SAR image of TC Joaquin; (**b**) the wind speed from the ECMWF reanalysis data; the retrieved wind speed by (**c**) SS-ICM model, (**d**) Shen model, (**e**) Horstmann model, (**f**) C3PO model, (**g**) the H14S model, (**h**) H14E model, and (**i**) MS1A model.

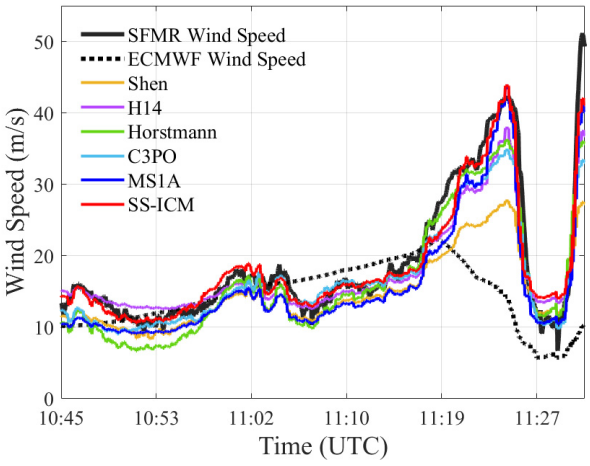

Figure 14. The comparison between the retrieved wind speeds and the wind speed from SFMR.

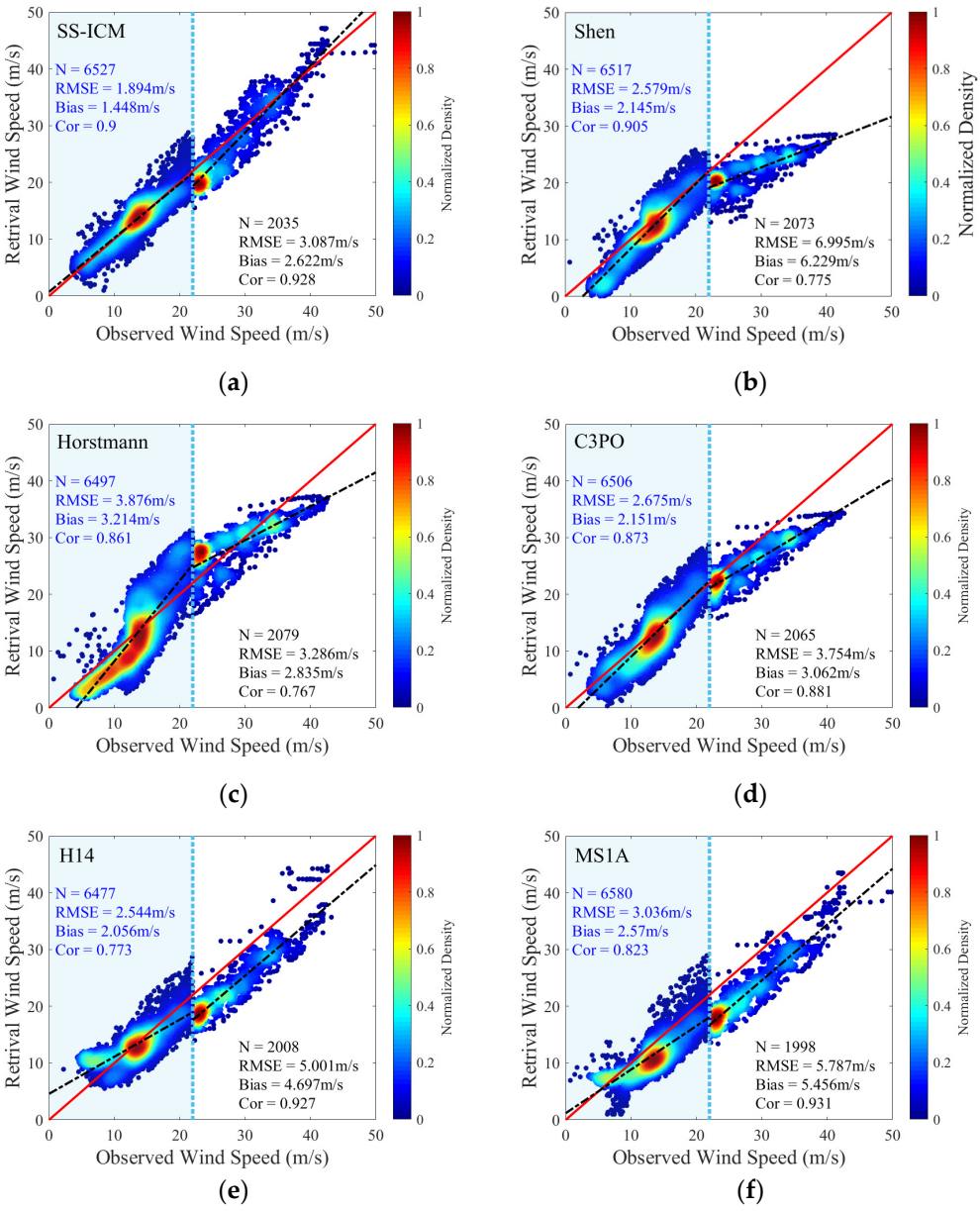

Figure 15. SAR-retrieved wind speeds (dataset B) by (**a**) the SS-ICM model; (**b**) the Shen model; (**c**) the Horstmann model; (**d**) the C3PO model; (**e**) the H14 model; (**f**) the MS1A model in vs. the ECMWF (with light blue background) and the SFMR wind speeds.

Table 5. Performances of wind speeds in dataset B vs. the results retrieved by the SS-ICM, Shen, Horstmann, C3PO, H14 and MS1A models.

Dataset B		SS-ICM	Shen	Horstmann	C3PO	H14	MS1A
ECMWF (<22 m/s)	RMSE (m/s)	1.894	2.579	3.876	2.675	2.544	3.036
	Bias (m/s)	1.448	2.145	3.214	2.151	2.056	2.570
	Cor	0.900	0.905	0.861	0.873	0.773	0.823
SFMR (≥22 m/s)	RMSE (m/s)	3.087	6.995	3.286	3.574	3.613	4.325
	Bias (m/s)	2.622	6.229	2.835	3.062	3.235	3.909
	Cor	0.928	0.775	0.767	0.881	0.927	0.926
All	RMSE (m/s)	2.258	3.547	3.708	2.945	2.838	3.361
	Bias (m/s)	1.739	2.831	3.104	2.355	2.340	2.872
	Cor	0.958	0.898	0.918	0.935	0.937	0.949

4.3.2. Comparison of Retrieval Results with the Wind Speed from SMAP

Among RS-2 datasets used in this paper, eight SAR images can be successfully matched with SMAP radiometer wind speeds. The wind speeds retrieved by the SS-ICM model are compared with the wind speeds from SMAP. For comparison, the retrieved wind speeds have been resampled to the spatial resolution of the SMAP data. In addition, because the MS1A model was established just based on the SMAP wind speeds, in this section, the MS1A model is chosen for comparison. Taking TC Joaquin and TC Florence as examples, Figure 16 shows the comparison between the retrieved wind speed and the SMAP data. The scatterplots of the retrieved wind speeds from SAR images are shown in Figure 17. As shown in Figure 17a, for the SS-ICM model, there is a strong correlation (0.955) between the retrieved wind speeds and the SMAP wind speed with RMSE of 2.816 m/s and bias of 2.149 m/s. The retrieved wind speeds by MS1A model have RMSE of 3.359 m/s, bias of 2.622 m/s, and a correlation coefficient of 0.949. The statistical results show that the SS-ICM model proposed in this paper has higher accuracy for the retrieval TC wind speeds. However, it should be noted that at the high wind speeds, the wind speeds retrieved by SS-ICM and MS1A are somewhat smaller than those acquired from SMAP, which may be caused by the influence of rainfall on C-band radar return signals. The influence of rainfall on cross-polarized NRCS is complex [40], which should be further studied in the future work.

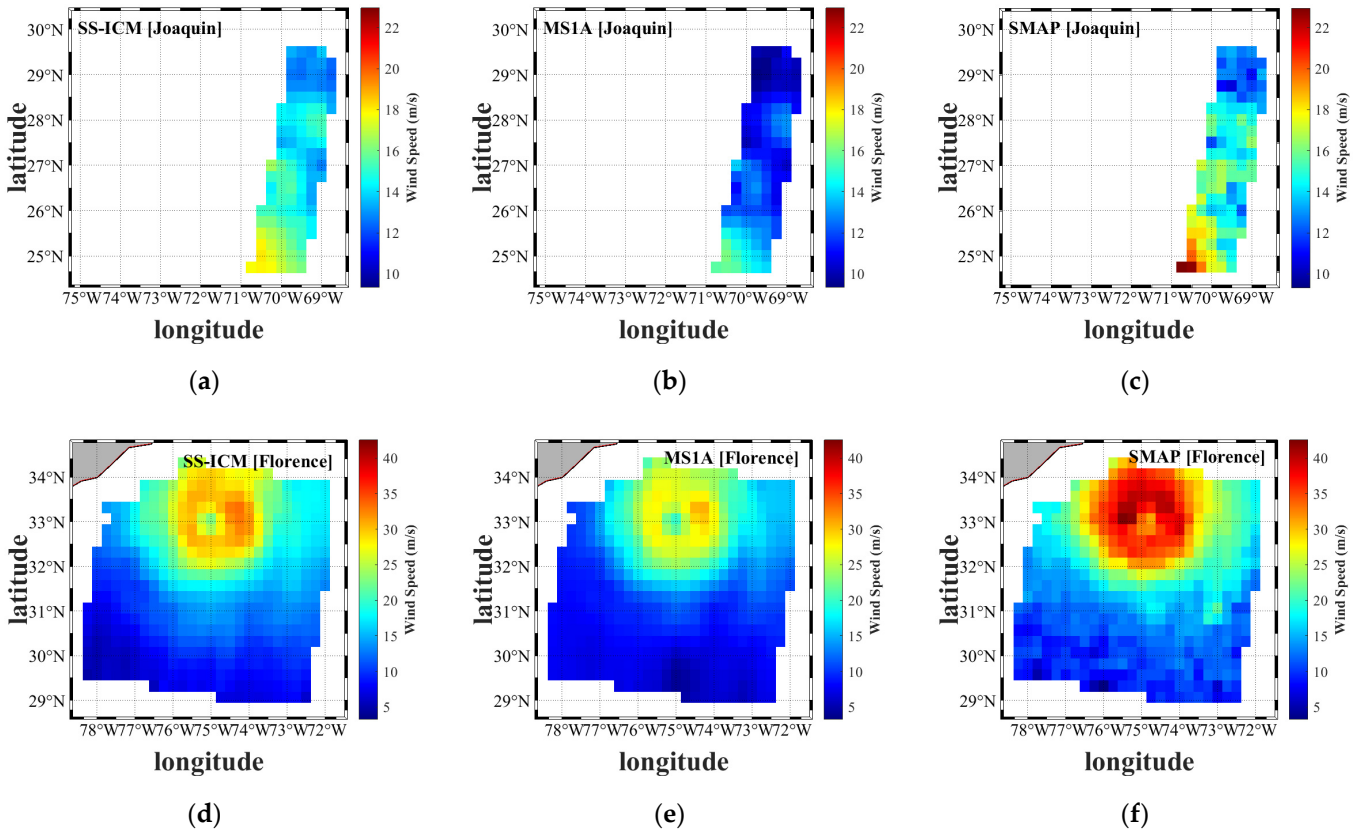

Figure 16. Wind speed retrieved by the SS-ICM, MS1A model, and wind speed from SMAP, corresponding to (**a**–**c**) TC Joaquin images and (**d**–**f**) TC Florence.

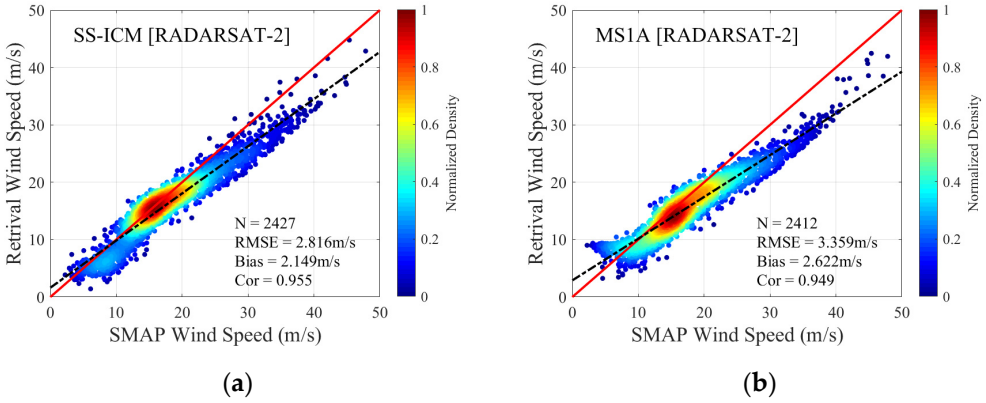

(**a**) (**b**)

Figure 17. Comparisons of retrieved wind speeds from RS-2 SAR with collocated SMAP wind speeds. (**a**) SS-ICM model. (**b**) MS1A model.

4.4. Universality Analysis of SS-ICM Model

In order to prove the applicability of SS-ICM model, 32 S-1 EW mode SAR images acquired over TCs were collected for retrieving wind speeds. The MS1A model was selected for comparison. As examples, the retrieved wind speeds for TC Kongney and TC Molave are shown in Figure 18. The scatterplots of the wind speeds retrieved from the collected S-1 SAR images are shown in Figure 19. Compared with the wind speed from SMAP, the retrieved wind speeds by SS-ICM have RMSE of 3.667 m/s, bias of 2.767 m/s, and a correlation coefficient of 0.929. For the wind speeds retrieved by MS1A, the RMSE, bias, and correlation coefficient are 4.911 m/s, 3.632 m/s, and 0.871, respectively. The results show that the SS-ICM model proposed in this paper can achieve adequate retrieval accuracy. Although SS-ICM model is established based on the RS-2 ScanSAR wide mode images and the wind speeds from ECMWF and SFMR, the successful applications to wind speed retrieval for different tropical cyclones in Figure 19 indicate that the SS-ICM model also has suitable adaptability for S-1 EW mode SAR images.

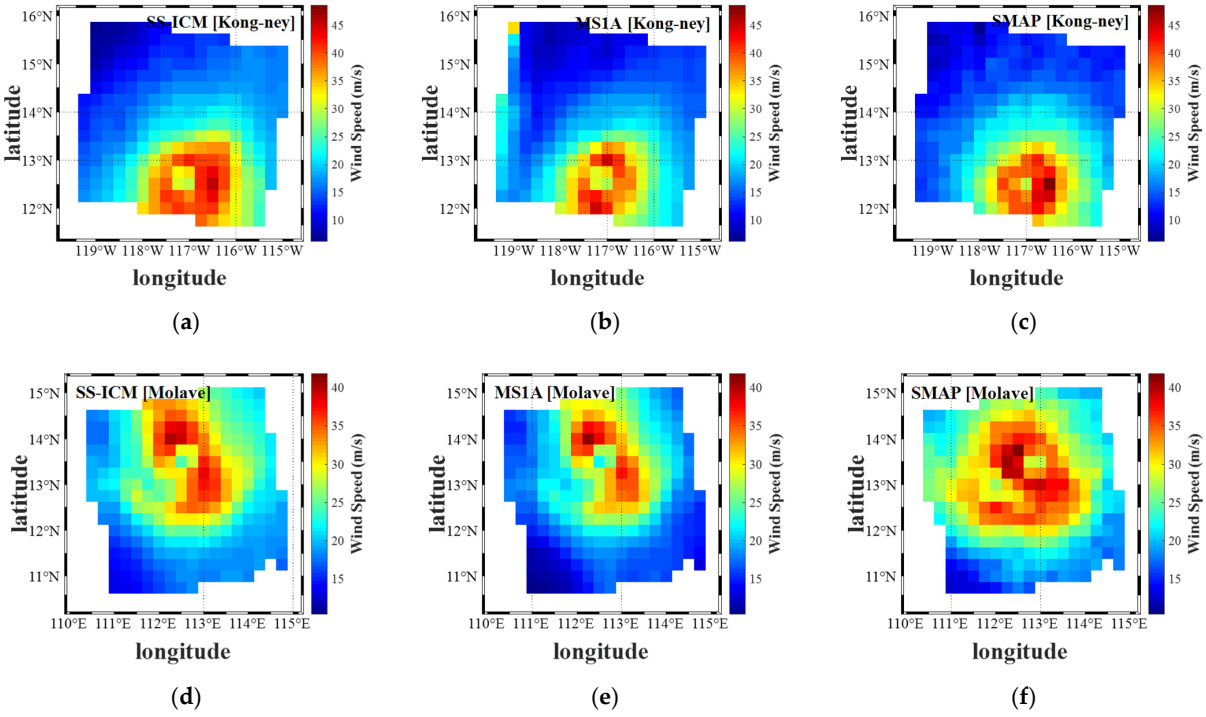

(**a**) (**b**) (**c**)

(**d**) (**e**) (**f**)

Figure 18. Wind speed retrieved by SS-ICM, MS1A model, and the wind speed from SMAP (**a**–**c**) corresponding to TC Kongney and (**d**–**f**) TC Molave.

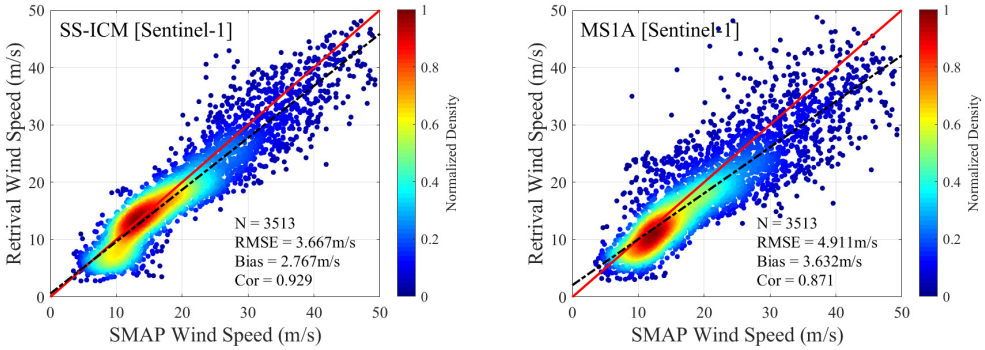

(**a**) (**b**)

Figure 19. Comparisons of retrieved wind speeds from S-1 SAR with collocated SMAP wind speed. (**a**) SS-ICM model. (**b**) MS1A model.

5. Conclusions

In this study, we developed a new GMF model for cross-polarized SAR images to retrieve sea surface wind speed. Sixteen RS-2 ScanSAR wide mode images under TC conditions and the collocated wind speeds from ECMWF, SFMR, and SMAP were collected and divided into datasets A and B. The SAR images and the matching wind speeds in dataset A were used to analyzing the influences of wind speed, wind direction, and radar incidence angle on the noise-free cross-polarized NRCS. The validity of the new GMF was verified by comparing the wind speeds retrieved from RS-2 images in dataset B with the matching wind speeds from ECMWF and SFMR. To further analyze the universality of the new GMF model, wind speed retrievals based on 32 S-1 EW mode SAR images were also compared with the matching wind speeds from SMAP. From the results in this work, the following conclusions are obtained.

Firstly, for RS-2 ScanSAR wide mode and S-1 EW mode SAR images, the cross-polarized NRCS was significantly contaminated by the reference noise. Therefore, the influence of the reference noise and the strip splicing lines should be removed before establishing the GMF model.

Secondly, the influences of the wind speed, wind direction, and radar incidence angle on the noise-free cross-polarized NRCS are analyzed according to dataset A. In addition to wind speed, SAR data indicate that radar incidence angle also has a non-negligible effect on the cross-polarized NRCS. The values of the cross-polarized NRCS for different wind speeds tend to decrease with the increase in incident angle. Nevertheless, the influence of the wind direction can be neglected. This means that the GMF is a function of wind speed and radar incidence angle.

Finally, a new GMF model (SS-ICM) for the cross-polarized NRCS was developed. As shown by SAR data, the cross-polarized NRCS monotonically increases with wind speeds. At moderate winds, the cross-polarized NRCS is most sensitive to wind speed. However, at lower and higher wind speeds, the values of the cross-polarized NRCS increase slowly with wind speed. Due to the complex trend of the cross-polarized NRCS with wind speed, three piecewise regression functions are given to quantify the relationship between cross-polarized NRCS and wind speed. In order to take the influence of incidence angle into account, the incidence angle correction functions for different sub-swaths were also introduced into the GMF model. The performance of the SS-ICM model was analyzed based on the wind speeds retrieved by different SAR datasets. From the comparisons with the retrieval results of other GMFs, the wind speed retrieved based on SS-ICM have the smallest RMSE and bias. The retrieval results were compared with the ECMWF wind speed below 22 m/s, and its RMSE was 1.894 m/s and bias was 1.448 m/s. Compared with the wind speed measured by SFMR above 22 m/s, the RMSE is 3.087 m/s, and the bias is 2.622 m/s. Compared with spaceborne L-band radiometers onboard SMAP data, this model still reaches a better retrieval accuracy. Accordingly, the applicability of the

SS-ICM model was analyzed by using 32 S-1 EW mode SAR images. Compared with SMAP wind speeds, the retrieved wind speeds have RMSE of 3.667 m/s and a bias of 2.767 m/s. Although SS-ICM model is established based on the RS-2 ScanSAR wide mode images, this model has suitable adaptability to S-1 EW mode SAR images, too.

Generally speaking, high wind speeds are usually accompanied by high rainfall. Compared to Ku-band, C-band data were reported to be far less affected by rain, about 1.5 dB [24,43], but small changes in NRCS would induce a significant impact on the high wind speed retrieved by SAR. In this paper, the influence of rainfall was not taken into account in the SS-ICM model, and the retrieved high wind speeds would be underestimated. The existence of atmospheric attenuation, body scattering, and ring wave makes the influence mechanism of rainfall on NRCS very complicated [39,40], which needs to be deeply studied in future work.

Author Contributions: Conceptualization, Y.Z. and Y.W.; Funding acquisition, Y.Z. and Y.W.; Methodology, L.L. and Y.W.; Validation, W.J.; Writing—original draft, L.L.; Writing—review and editing, Y.Z., Y.W. and D.S. All authors have read and agreed to the published version of the manuscript.

Funding: This research was funded by the National Natural Science Foundations of China (41976167, 41576170), the Key Research and Development Program of Shandong Province (International Science and Technology Cooperation) (2019GHZ023), and Shandong Provincial Natural Science Foundation (ZR2021MD023).

Institutional Review Board Statement: Not applicable.

Informed Consent Statement: Not applicable.

Data Availability Statement: ECMWF-ERA5 wind speed data can download from the website https://cds.climate.copernicus.eu/cdsapp#!/search?type=dataset, accessed data: 20 November 2021. SFMR measurements of wind speed were provided by NOAA Hurricane Research Division (HRD) (https://www.aoml.noaa.gov/hrd/data_sub/hurr.html), accessed data: 23 November 2021. L-band SMAP wind speed data can be obtained at https://www.remss.com/missions/SMAP/winds/, accessed data: 13 March 2022. IBTrACS_v04 dataset is provided by NOAA (https://www.ncdc.noaa.gov/ibtracs/index.php?name=ib-v4-access), accessed data: 8 October 2021.

Conflicts of Interest: The authors declare no conflict of interest.

References

1. Shahrezaei, I.H.; Kim, H.C. A Novel SAR Fractal Roughness Modeling of Complex Random Polar Media and Textural Synthesis Based on a Numerical Scattering Distribution Function Processing. *IEEE J. Sel. Top. Appl. Earth Obs. Remote Sens.* **2021**, *14*, 7386–7409. [CrossRef]
2. Wang, C.; Zheng, G.; Li, X.; Xu, Q.; Liu, B.; Zhang, J. Tropical cyclone intensity estimation from geostationary satellite imagery using deep convolutional neural networks. *IEEE Trans. Geosci. Remote Sens.* **2021**, *60*, 1–16. [CrossRef]
3. Zhang, B.; Zhu, Z.; Perrie, W.; Tang, J.; Zhang, J.A. Estimating tropical cyclone wind structure and intensity from spaceborne radiometer and synthetic aperture radar. *IEEE J. Sel. Topics Appl. Earth Observ.* **2021**, *14*, 4043–4050. [CrossRef]
4. Zhao, Y.; Mouche, A.A.; Chapron, B.; Reul, N. Direct comparison between active C-band radar and passive L-band radiometer measurements: Extreme event cases. *IEEE Geosic. Remote Sens. Lett.* **2018**, *15*, 897–901. [CrossRef]
5. Bentamy, A.; Grodsky, S.; Carton, J.; Croizé-Fillon, D.; Chapron, B. Matching ASCAT and QuikSCAT winds. *J. Geophys. Res. Oceans.* **2012**, *117*, C2. [CrossRef]
6. Meissner, T.; Ricciardulli, L.; Manaster, A. Tropical Cyclone Wind Speeds from WindSat, AMSR and SMAP: Algorithm Development and Testing. *Remote Sens.* **2021**, *13*, 1641. [CrossRef]
7. Quilfen, Y.; Vandemark, D.; Chapron, B.; Feng, H.; Sienkiewicz, J. Estimating gale to hurricane force winds using the satellite altimeter. *J. Atoms. Ocean. Techol.* **2011**, *28*, 453–458. [CrossRef]
8. Landy, J.C.; Tsamados, M.; Scharien, R.K. A facet-based numerical model for simulating SAR altimeter echoes from heterogeneous sea ice surfaces. *IEEE Trans. Geosci. Remote Sens.* **2019**, *57*, 4164–4180. [CrossRef]
9. Ardhuin, F.; Stopa, J.; Chapron, B.; Collard, F.; Husson, R.; Jensen, R.E.; Johannessen, J.; Mouche, A.; Passaro, M.; Quartly, G.; et al. Observing sea states. *Front. Mar. Sci.* **2019**, *6*, 124. [CrossRef]
10. Mouche, A.; Chapron, B. Global C-B and Envisat, RADARSAT-2 and Sentinel-1 SAR measurements in copolarization and cross-polarization. *J. Geophys. Res. Oceans* **2015**, *120*, 7195–7207. [CrossRef]
11. Mouche, A.A.; Chapron, B.; Zhang, B.; Husson, R. Combined co- and cross-Polarized SAR measurements under extreme wind conditions. *IEEE Trans. Geosci. Remote Sens.* **2017**, *55*, 6746–6755. [CrossRef]

12. Zhang, B.; Perrie, W.; Vachon, P.W.; Li, X.; Pichel, W.G.; Guo, J.; He, Y. Ocean vector winds retrieval from C-band fully polarimetric SAR measurements. *IEEE Trans. Geosci. Remote Sens.* **2012**, *50*, 4252–4261. [CrossRef]
13. Stoffelen, A.; Verspeek, J.A.; Vogelzang, J.; Verhoef, A. The CMOD7 geophysical model function for ASCAT and ERS wind retrievals. *IEEE J. Sel. Topics. Appl. Earth. Observ.* **2017**, *10*, 2123–2134. [CrossRef]
14. Iervolino, P.; Guida, R.; Whittaker, P. Roughness parameters estimation of sea surface from SAR images. In Proceedings of the 2014 IEEE Geoscience and Remote Sensing Symposium, IGARSS, Quebec City, QC, Canada, 13–18 July 2014.
15. Zhou, X.; Chong, J.; Bi, H.; Yu, X.; Shi, Y.; Ye, X. Directional spreading function of the gravity-capillary wave spectrum derived from radar observations. *Remote Sens.* **2017**, *9*, 361. [CrossRef]
16. Hwang, P.A.; Zhang, B.; Perrie, W. Depolarized radar return for breaking wave measurement and hurricane wind retrieval. *Geophys. Res. Lett.* **2010**, *37*, 70–75. [CrossRef]
17. Kudryavtsev, V.; Kozlov, I.; Chapron, B.; Johannessen, J.A. Quad-polarization SAR features of ocean currents. *J. Geophys. Res. Oceans* **2014**, *119*, 6046–6065. [CrossRef]
18. Hwang, P.A.; Fois, F. Surface roughness and breaking wave properties retrieved from polarimetric microwave radar backscattering. *J. Geophys. Res. Oceans* **2015**, *120*, 3640–3657. [CrossRef]
19. Kudryavtsev, V.N.; Fan, S.; Zhang, B.; Mouche, A.A.; Chapron, B. On quad-polarized SAR measurements of the ocean surface. *IEEE Trans. Geosci. Remote Sens.* **2019**, *57*, 8362–8370. [CrossRef]
20. Zhang, B.; Perrie, W.; He, Y. Wind speed retrieval from RADARSAT-2 quad-polarization images using a new polarization ratio model. *J. Geophys. Res. Oceans* **2011**, *116*, C8. [CrossRef]
21. Vachon, P.W.; Wolfe, J. C-Band cross-polarization wind speed retrieval. *IEEE Geosic. Remote Sens. Lett.* **2011**, *8*, 456–459. [CrossRef]
22. Zhang, B.; Perrie, W. Cross-polarized synthetic aperture radar: A new potential measurement technique for hurricanes. *Bull. Amer. Meteorol. Soc.* **2012**, *93*, 531–541. [CrossRef]
23. Zhang, B.; Perrie, W.; Zhang, J.A.; Uhlhorn, E.W.; He, Y. High-resolution hurricane vector winds from C-band dual-polarization SAR Observations. *J. Atoms. Ocean. Technol.* **2014**, *31*, 272–286. [CrossRef]
24. Zadelhoff, G.V.; Stoffelen, A.; Vachon, P.W.; Wolfe, J.; Horstmann, J.; Belmonte Rivas, M. Scatterometer hurricane wind speed retrievals using cross polarization. *Atmos. Meas. Tech. Discuss.* **2013**, *6*, 7945–7984.
25. Hwang, P.A.; Stoffelen, A.; Zadelhoff, G.V.; Perrie, W.; Zhang, B. Cross-polarization geophysical model function for C-band radar backscattering from the ocean surface and wind speed retrieval. *J. Geophys. Res. Oceans* **2015**, *120*, 893–909. [CrossRef]
26. Zhang, G.; Li, X.; Perrie, W.; Hwang, P.A.; Zhang, B.; Yang, X. A hurricane wind speed retrieval model for C-band RADARSAT-2 cross-polarization ScanSAR images. *IEEE Trans. Geosci. Remote Sens.* **2017**, *55*, 4766–4774. [CrossRef]
27. Mouche, A.; Chapron, B.; Knaff, J.; Zhao, Y.; Zhang, B.; Combot, C. Copolarized and cross-polarized SAR measurements for high-resolution description of major hurricane wind structures: Application to Irma category 5 hurricane. *J. Geophys. Res. Oceans* **2019**, *124*, 3905–3922. [CrossRef]
28. Shen, H.; Perrie, W.; Liu, G. Wind speed retrieval from VH dual-polarization RADARSAT-2 SAR Images. *IEEE Trans. Geosci. Remote Sens.* **2014**, *52*, 5820–5826. [CrossRef]
29. Horstmann, J.; Caruso, M.J.; Wackerman, C.; Falchetti, S.; Maresca, S. Tropical cyclone winds retrieved from C-band cross-polarized synthetic aperture radar. *IEEE Trans. Geosci. Remote Sens.* **2015**, *53*, 2887–2898. [CrossRef]
30. MacDonald. *RADARSAT-2 Product Description*; Tech. Rep. RN-SP-52-1238; Dettwiler Assoc.: Richmond, BC, Canada, 2014.
31. Hersbach, H. Comparison of C-Band scatterometer CMOD5.N equivalent neutral winds with ECMWF. *J. Atoms. Ocean. Technol.* **2010**, *27*, 721–736. [CrossRef]
32. Ge, C. An intercomparison of TOPEX, NSCAT, and ECMWF wind speeds: Illustrating and understanding systematic discrepancies. *Monthly Weather Rev.* **2010**, *132*, 780–792.
33. Szczypta, C.; Calvet, J.C.; Albergel, C.; Balsamo, G.; Meurey, C. Verification of the new ECMWF ERA-Interim reanalysis over France. *Hydrol. Earth. Syst. Sc.* **2011**, *15*, 647–666. [CrossRef]
34. Hennermann, K.; Berrisford, P. ERA5 Data Documentation. *Copernic. Knowl. Base*. **2017**. Available online: https://confluence.ecmwf.int/display/CKB/ERA5%3A+data+documentation (accessed on 24 March 2022).
35. Franklin, J.L.; Black, M.L.; Valde, K. GPS dropwindsonde wind profiles in hurricanes and their operational implications. *Weather Forecast.* **2002**, *18*, 32–44. [CrossRef]
36. Uhlhorn, E.W.; Black, P.G. Verification of remotely sensed sea surface winds in hurricanes. *J. Atoms. Ocean. Technol.* **2003**, *20*, 99–116. [CrossRef]
37. Uhlhorn, E.W.; Black, P.G.; Goodberlet, M.; Franklin, J.L. Hurricane surface wind measurements from an operational Stepped Frequency Microwave Radiometer. *Monthly Weather Rev.* **2007**, *135*, 3070–3085. [CrossRef]
38. Klotz, B.W.; Uhlhorn, E.W. Improved Stepped Frequency Microwave Radiometer tropical cyclone surface winds in heavy Precipitation. *J. Atmos. Oceanic Technol.* **2014**, *31*, 2392–2408. [CrossRef]
39. Zhao, X.B.; Shao, W.Z.; Zhao, L.B.; Gao, Y.; Yuan, X.Z. Impact of rain on wave retrieval from Sentinel-1 synthetic aperture radar images in tropical cyclones. *Adv. Space Res.* **2021**, *67*, 3072–3086. [CrossRef]
40. Zhang, G.; Li, X.F.; Perrie, W.; Zhang, B.; Wang, L. Rain effects on the hurricane observations over the ocean by C-band Synthetic Aperture Radar. *J. Geophys. Res. Oceans* **2016**, *121*, 14–26. [CrossRef]
41. Entekhabi, D.; Njoku, E.G.; O'Neill, P.; Kellogg, K.H.; Crow, W.; Edelstein, W.N.; Entin, J.K.; Goodman, S.D.; Jackson, T.J.; Johnson, J.; et al. The Soil Moisture Active Passive (SMAP) mission. *Proc. IEEE* **2010**, *98*, 704–716. [CrossRef]

42. Brown, M.E.; Escobar, V.; Moran, S.; Entekhabi, D.; O'Neill, P.E.; Njoku, E.G.; Doorn, B.; Entin, J.K. NASA's soil moisture active passive (SMAP) mission and opportunities for applications users. *Bull. Am. Meteorol. Soc.* **2013**, *94*, 1125–1127. [CrossRef]
43. Meissner, T.; Ricciardulli, L.; Wentz, F.J. Capability of the SMAP Mission to Measure Ocean Surface Winds in Storms. *Bull. Am. Meteor. Soc.* **2017**, *98*, 1660–1677. [CrossRef]
44. Yueh, S.H.; Fore, A.G.; Tang, W.; Hayashi, A.; Stiles, B.; Reul, N. SMAP L-Band Passive Microwave Observations of Ocean Surface Wind during Severe Storms. *IEEE Trans. Geosci. Remote* **2016**, *54*, 7339–7350. [CrossRef]
45. Sun, Z.; Zhang, B.; Zhang, J.A. Examination of Surface Wind Asymmetry in Tropical Cyclones over the Northwest Pacific Ocean Using SMAP Observations. *Remote Sens.* **2019**, *11*, 2604. [CrossRef]
46. Kenneth, R.K.; Michael, C.K.; David, H.L.; Howard, J.D.; Charles, J.N. The international best track archive for climate stewardship (IBTrACS) unifying tropical cyclone data. *Bull. Am. Meteorol. Soc.* **2010**, *91*, 363–376.
47. Kishtawal, C.M.; Jaiswal, N.; Singh, R.; Niyogi, D. Tropical cyclone intensification trends during satellite era (1986–2010). *Geophys. Res. Lett.* **2012**, *39*, 10810. [CrossRef]
48. Kieran, T.B.; Gabriel, A.V.; Thomas, R.K.; Hiroyuki, M. Recent increases in tropical cyclone intensification rates. *Nat. Commun.* **2019**, *10*, 635.